RSC Advances

PAPER

View Article Online
View Journal | View Issue

Cite this: *RSC Adv.*, 2017, 7, 6842

Novel fungal hyphae/Fe_3O_4 and N-TiO_2/NG composite for adsorption and photocatalysis

Yiren lian,[ab] Xueyuan Bai,[c] Xueqian Li,[d] Zhan Gao,[e] Zuowen Hu*[b] and Guozhen Hu*[b]

Received 28th October 2016
Accepted 29th December 2016

DOI: 10.1039/c6ra25964b

www.rsc.org/advances

Nano TiO_2 particles are applied in photocatalysis but are difficult to recycle. Meanwhile, low light transmission and a lack of oxygen in solution also causes a decrease in photocatalytic efficiency. Here, we prepare a mycelium pellet to anchor TiO_2 particles, which can float on the surface of aqueous solutions and enrich organic materials. The mycelium pellet is a three-layered sphere, in which the innermost layer is fungal hyphae, the middle layer is fungal hyphae/Fe_3O_4, and the outer layer is fungal hyphae/N-TiO_2/NG. In comparison to TiO_2 particles, the mycelium pellet is not only convenient to recycle, but can also easily receive light and oxygen. The results of adsorption and photocatalytic activity tests clearly indicate that the floatable mycelium pellet could be a potential photocatalytic material for practical applications.

1. Introduction

Recently, photocatalysis has received intensive attention as an ideal method to control pollution in organic wastewater by the utilization of light energy. Among various photocatalysts, titanium dioxide (TiO_2) has been widely investigated due to its superior properties, such as high chemical stability, high cost-efficiency, exceptional optoelectronic properties, and non-toxicity.[1–4] However, while TiO_2 is easily dispersed in solution, it is difficult to separate from a solution, causing secondary dust pollution. Therefore, it is essential to search for ways to fabricate macro-scale TiO_2 composites to realize its practical application.

Fungal hyphae (FH) as a kind of filamentous microorganism, which possesses extremely strong vitality and reproductive capacity, can grow rapidly within several days from single cells to a macro-scale microbe, with a length of a centimetre and a diameter less than 10 μm.[5,6] Therefore, it can be easily available in large quantities, facilitating its practical application. Moreover, the advantages of its low cost, environmental friendliness and unique structure have led to a considerable amount of research. The superiority of biomass carriers makes them suitable for use in the fabrication of new biocomposites for application in many fields, such as batteries,[7,8] catalysis,[9,10] wastewater treatment,[11,12] and in the synthesis of various noble metal nanoparticles.[13–15] Thus, fungal hyphae, as a template for the loading of TiO_2 nanoparticles, may address the above issue. This is feasible because TiO_2 can easily anchor on the cell walls of fungal hyphae, building a bridge between the micro and macro worlds due to bonding with large quantities of functional groups, such as phosphonate, hydroxyl, and amine groups.[16] Besides, the high adsorption capacity of FH is beneficial to the efficiency of photocatalysis, and the combination of FH and TiO_2 may result in a synergistic effect. Nevertheless, only a small quantity of TiO_2 can be attached to the surface of fungal hyphae due to the lack of active sites.

Graphene (Gr, two-dimensional planar structure) has a high specific surface area and abundant active sites.[17] Therefore, Gr is expected to work as a platform for loading TiO_2 and connecting with fungal hyphae. Moreover, the combination of TiO_2 and graphene also generates a synergistic effect to improve photocatalytic activity by enhancing the adsorption and charge transfer rate.[18,19] In order to enhance the sensitivity of TiO_2 to visible light, nitrogen-doping could be adopted to increase the visible-light response of TiO_2.[20] According to previous reports, a combination of N-doped TiO_2 and graphene (NTG) exhibited a higher photocatalytic activity than single nitrogen-doping or the introduction of graphene under visible light.[21]

Magnetic collection is a simple and efficient approach to separate a catalyst from solution. Fe_3O_4 nanoparticles have been widely studied for wastewater treatment due to their excellent magnetic behaviour.[22–24] For example, a new adsorbent consisting of nano-Fe_3O_4 and polymer was reported for the removal of Cr(VI), which is easily separated from solution with magnetic nanoparticles.[25] Therefore, we introduced nano-Fe_3O_4 for better recycling of FMT. In this work, FMT was successfully synthesized with FH, nano-Fe_3O_4, and NTG by a simple co-

---

[a] Graduate School of CAEP, Mianyang, Sichuan, 621900, China

[b] CAEP Institute of Technology, Miangyang, Sichuan, 621900, China. E-mail: ZuowenHu2000@hotmail.com

[c] Laboratory of Extreme Conditions Matter Properties, Southwest University of Science and Technology, Mianyang, 621010, China

[d] State Key Laboratory of Clean Energy Utilization, Zhejiang University, Hangzhou, 31000, China

[e] Key Lab. for Power Machinery and Engineering of M. O. E., Shanghai Jiao Tong University, Shanghai, 200240, China

culture method. After freeze drying and heating at 90 °C, FMT could be suspended on the surface of a solution, and thus easily received light and oxygen compared to membranes or powdered materials, which reacted in solution. Moreover, it could also be easily oriented and separated from the solution under an applied magnetic field due to its magnetic properties. Tannin was selected as a typical organic material to investigate the adsorption ability and photocatalytic activity under simulated solar light irradiation.

2. Experimental section

2.1 Materials

The fungus (penicillium) was purchased from the Microbiology Department of East China Institute of Technology. Graphite powder (≥99.85% purity) was purchased from Shanghai Huayi Group Company. $Ti(SO_4)_2 \cdot 9H_2O$ (≥96.4% purity) was purchased from Sinopharm Chemical Reagent Co., Ltd. All other chemicals of analytical grade were available from Chengdu Kelong Chemical Co., Ltd. All solutions were prepared using Milli-Q water and analytical grade chemicals.

2.2 Synthesis of FMT

A schematic diagram of the synthesis route is shown in Scheme 1a. First of all, the magnetic nanoparticles were prepared by a co-precipitation method.[26] Briefly, 8.11 g $FeCl_3 \cdot 6H_2O$, 2.98 g $FeCl_2 \cdot 4H_2O$, and 5.85 g NaCl were added to 400 mL deionized water. Then, 100 mL of 1 mol L^{-1} NaOH solution was added gradually to the mixed solution under magnetic stirring and N_2 (g) atmosphere. After that, nano-Fe_3O_4 particles were separated with a strong magnet. Nano-Fe_3O_4 particles were washed with deionized water and centrifuged at 4000 rpm three times. Finally, the magnetic nanoparticles were freeze-dried for future use.

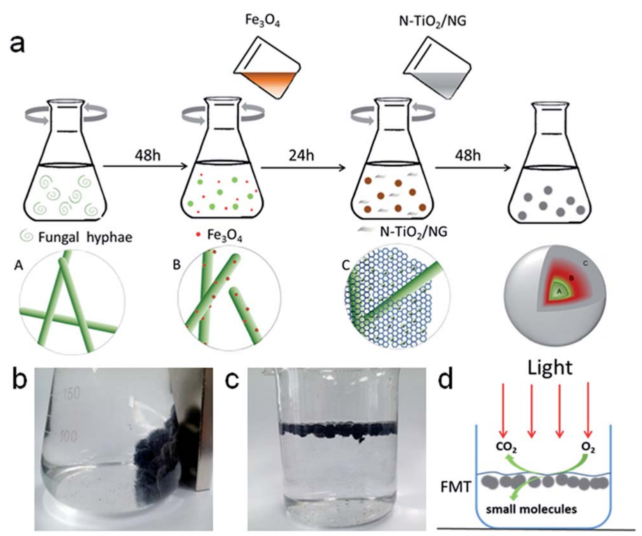

Scheme 1 (a) Route diagram for synthesizing FMT hydrogel; (b) an image of magnetic FMT hydrogel; (c) FMT hydrogel suspended in water after freeze drying and heating; (d) diagram of tannin degradation by FMT.

The NTG composite was prepared as follows. First, GO solution (0.6 mg L^{-1}) was prepared from graphite powder by a modified Hummers method.[27] The as-prepared GO solution was first sonicated for 0.5 h, and then 65 mL GO solution, 5 mL NH_3 (pure 25–28%), and 1 g $Ti(SO_4)_2 \cdot 9H_2O$ were mixed in a 100 mL Teflon-lined stainless steel autoclave under vigorous stirring at room temperature. After that, the mixture was heated at 160 °C for 20 h in an oven and cooled down to room temperature, and the black precipitate in the autoclave was treated by centrifugation and washing several times. Finally, the sample was further dispersed under ultrasound.

FTM was synthesized with FH, as-prepared Fe_3O_4, and NTG by a co-culture method. Spores of fungus and 150 mL of medium (containing 2% glucose, 0.25% yeast, 0.25% peptone) were added to a 250 mL flask and grown in a rotary shaker with a shake rate of 130 rpm at 30 °C for 48 h. Then, about 0.2 g nano-Fe_3O_4 particles were added to the suspensions mentioned above, and the mixed solutions were cultivated in the rotary shaker again for 24 h. Next, excess NTG was added to the mixture and grown for another 48 h. Finally, the obtained composites were washed several times with deionized water to remove superfluous organic material and particles. The magnetic FMT hydrogel can be seen in Scheme 1b. The composite was freeze-dried, and then heated at 90 °C for 24 hours. FMT aerogel is shown floating in aqueous solution in Scheme 1c. This can easily receive light and oxygen on the surface of water, and tannin can be effectively degraded into small molecules, such as CO_2 and H_2O, under simulated solar light (Scheme 1d).

2.3 Characterization

The surface morphology of samples was characterized by scanning electron microscopy (SEM, Zeiss Ultra 55). The crystalline phases were identified with an X-ray diffractometer (PANalytical, Netherlands) with Cu-Kα radiation ($\lambda = 1.5406$ Å). The surface functional groups were identified by Raman spectroscopy and Fourier transform infrared spectroscopy (FTIR, PE Spectrum One), and the elementary compositions and bonding energies were analyzed by X-ray photoelectron spectroscopy (XPS, SSX-100). The band gaps of compound semiconductors were estimated with a UV-visible spectrophotometer (UV-3150, Shimadzu, Japan) with a diffuse reflectance accessory.

2.4 Adsorption and photocatalytic measurement

Adsorption experiments were conducted in a 200 mL beaker under magnetic stirring and kept in the dark; 50 mg FMT, 5 mg tannin, and 100 mL deionized water were added to the beaker (room temperature, pH = 6.5 (±0.1), $m/V = 0.5$ g L^{-1}). The mixed solution was measured hourly with a UV2600A spectrophotometer. Photocatalytic testing was carried out in a 500 mL beaker, to which was added 0.5 g sample, 300 mL deionized water, and 30 mg tannin. The mixture was placed in the dark to reach an equilibrium concentration of tannin. Then, the reaction mixture was irradiated with light (xenon lamp, 500 W) and kept standing. The reaction mixture was collected to be measured half-hourly with the UV2600A spectrophotometer.

The concentration of tannin was analysed with the UV2600A spectrophotometer at 215 nm.

3. Results and discussion

3.1 Characterization

Photographs of the FH and FMT hydrogels are respectively shown in Fig. 1a and b. These are spherical and the size of the spheres was about 1 cm. The surface colour of FMT is clearly different from that of the FH surface, indicating a possible coating of NTG on FH. An SEM image of the surface morphology of FH is shown in Fig. 1c. FH is composed of numerous micron-sized filamentous biomasses and a handful of biomass mucosa, which are crisscrossed and distributed irregularly in the space. Nevertheless, Fig. 1d shows that the structure of the FMT surface is covered with abundant sheets, which are considered to be NTG, and little fungal hyphae are exposed on the surface. In order to clearly identify the sheets and understand the structure, higher resolution images of the FH and FMT surfaces have been obtained. The higher resolution image of fungal hyphae shown in Fig. 1e indicates that the diameter of the fungal hyphae is about 2.5 μm and that their surface is smooth. On the contrary, Fig. 1f shows that the surface of FMT is filled with different sized sheets whose structure is similar to that of GO sheets.

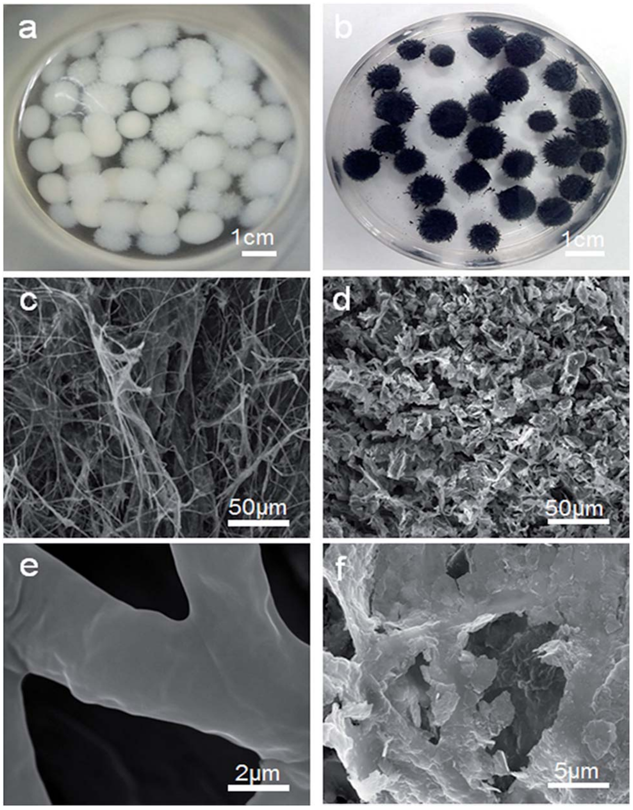

Fig. 1 Digital photos of the samples: (a) pure fungus and (b) FMT composite; SEM images of (c and e) pure fungus and (d and f) the surface of FMT composite.

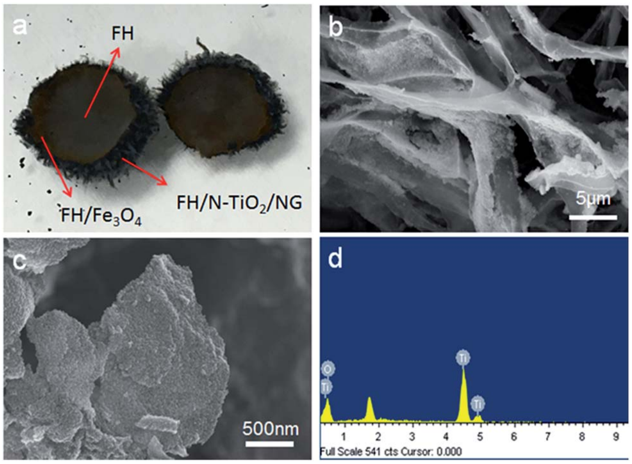

Fig. 2 (a) A digital photo of an FTM cross-section; (b) an SEM image of the Fe_3O_4/fungus structure; (c) a high-resolution image of the FMT composite surface; (d) EDS measurement of a sheet on the surface of FMT.

As shown in Fig. 2a, the cross-sectional structure of FTM hydrogel shows the three-layered structure of FMT. The middle layer is believed to consist of Fe_3O_4 nanoparticles and fungal hyphae, and this can be confirmed with Fig. 2b, which shows that the Fe_3O_4 nanoparticles adhere to the surface of FH and biomass mucosa. The outer layer is composed of N-TiO_2/NG and fungus. As shown in Fig. 2c, a sheet from the surface of FMT is evenly covered with a large number of small particles, which are believed to be TiO_2 nanoparticles, and the EDS measurement (Fig. 2d) reveals that the main elements are Ti and O, confirming the coverage of TiO_2 nanoparticles on graphene sheets.

Fig. 3a shows a TEM image of NTG in the FMT composite. TiO_2 is successfully coated and anchored on GO by chemical bonds, such as Ti–C or Ti–O–C, after the hydrothermal reaction. Meanwhile, the crystallite sizes of TiO_2 were also investigated by high-resolution transmission electron microscopy (HRTEM), as shown in Fig. 3b. The sizes of the TiO_2 particles are around

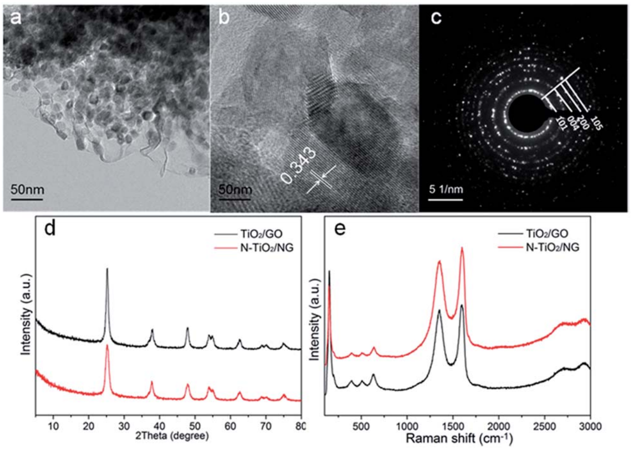

Fig. 3 (a) TEM image, (b) HRTEM image and (c) SAED pattern of NTG composites; (d) XRD patterns of TiO_2/GO and NTG; (e) Raman spectra of TiO_2/GO and NTG.

10 nm and the interplanar spacings of TiO_2 nanoparticles were calculated as 0.343 nm, corresponding to the (101) crystallographic planes of anatase TiO_2. Furthermore, a selected area electron diffraction (SAED) pattern of NTG (Fig. 3c) displayed a series of discontinuous Debye–Scherrer rings, which corresponded to the (101), (004), (200), and (105) phases of anatase TiO_2. Fig. 3d shows the crystalline phases of TiO_2/GO and NTG. It can be seen that the peaks of TiO_2/GO and NTG are similar and no crystalline phase related to nitrogen was found. The peaks are exactly consistent with the crystal planes (JCPDS, no. 21-1272). It is noted that the absence of the peak at 10.8° implies that GO was successfully reduced to graphene. Nevertheless, the peak of graphene expected at about 26° is not present. It can be shown that the TiO_2 anchored on graphene resulted in a high intensity peak, which covered that of graphene.[28] Fig. 3e displays the Raman spectra of TiO_2/GO and NTG. Peaks related to the anatase phases,[29] 148 (E_g), 198 (E_g), 395 (B_{1g}), 510 (A_{1g}), and 628 (E_g) cm^{-1} are observed in the Raman spectra. In addition, the peaks at 1355 and 1596 cm^{-1} represent the D and G bands, respectively. The D band indicates the presence of sp^3 defects and structural disorder in graphene, while the G band is common to sp^2-hybridized C=C.[30] The intensity ratios of the D/G bands for TiO_2/GO and NTG (1.00 and 1.12, respectively) are higher than that of GO reported in a preview paper, which confirms the presence of graphene sheets in TiO_2/GO and NTG composites.[31]

As shown in Fig. 4a, the XPS survey spectra indicate that the main components of TiO_2/GO and NTG are Ti, O, and C. The peak at around 400 eV, corresponding to N 1s, indicates that nitrogen is doped in the TiO_2/GO composite and the elementary compositions of NTG, for Ti, O, C, and N, are 20.22 atom%, 29.75 atom%, 47.35 atom%, and 2.68 atom%, respectively. Fig. 4b shows a comparison of TiO_2/GO and NTG with Ti 2p high-resolution XPS spectra. Compared with TNTs/GO at 458.9 and 465.1 eV, the bonding energies of NTG show a shift to lower energies. This is because the nitrogen is incorporated into the TiO_2 lattice and replaces the oxygen atoms, leading to lower binding energies.[32,33] The C 1s high-resolution XPS spectrum of NTG is displayed in Fig. 4c. It should be resolved into four peaks assigned to C=C, C–O, C=O and Ti–O–C. However, the positions of the bonding energies can not match with C=C, C–O, C=O and Ti–O–C. This is due to the doping of nitrogen into graphene causing the change of the bonding energies. Therefore, it is resolved into four peaks at 284.7 eV (C=C), 285.3 eV (C=N/C–O), 286.7 eV (C–N/C=O) and 288.9 eV (N–C=O/Ti–O–C), and no peak appeared at 281 eV which represents Ti–C bond indicating that carbon was not doped into the TiO_2 lattice.[34–36] Moreover, the N 1s spectrum of NTG (Fig. 4d) is deconvolved into three peaks at 398.5, 400, and 401.6 eV, which are assigned to Ti–N/pyridinic N, pyrrolic N/O–Ti–N, and quaternary N. This further suggests the doping of N into TiO_2/GO.

The optical properties of TiO_2/GO and NTG were investigated with UV-vis diffuse reflectance spectra. As shown in Fig. 5a, it is observed that TiO_2/GO and NTG both show a low reflectance in the ultraviolet and visible light regions. The corresponding plots of $[F(R)h\nu]^{1/2}$ *vs.* $h\nu$ are displayed in Fig. 5b. The band gap energies are estimated from the extrapolated value from UV-vis diffuse reflectance spectroscopy, and the result indicates that the values for TiO_2/GO and NTG are 2.96 and 2.59 eV, respectively. Comparing TiO_2/GO and NTG indicates that the introduction of nitrogen causes narrowing of the band gap.

The FTIR spectra of FH, FH–tannin, FH/Fe_3O_4, and FH/NTG are shown in Fig. 5c. Various functional groups can be found in the FTIR spectrum of fungal hyphae. It can be observed that the characteristic bands correspond to O–H and N–H at 3400 cm^{-1}, –CH, –CH_2, and –CH_3 at ~2900 cm^{-1}, C=O stretching (amide I) and –NH_2 related to proteins at ~1650 cm^{-1}, N–H and C–N stretching related to proteins (amide II) at ~1540 cm^{-1}, and C–OH associated with phosphorylated proteins and alcohols at ~1050 cm^{-1}.[37,38] The similarity of the FTIR spectra of FH and FH/Fe_3O_4 indicates that the main functional groups remain.

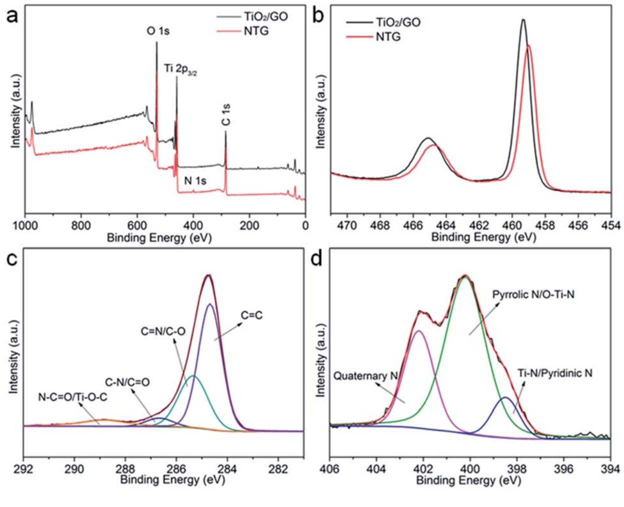

Fig. 4 (a) Survey XPS spectra of TiO_2/GO and NTG; (b) high-resolution Ti 2p core level XPS spectra of TiO_2/GO and NTG; (c and d) high-resolution C 1s and N 1s core level XPS spectra of NTG.

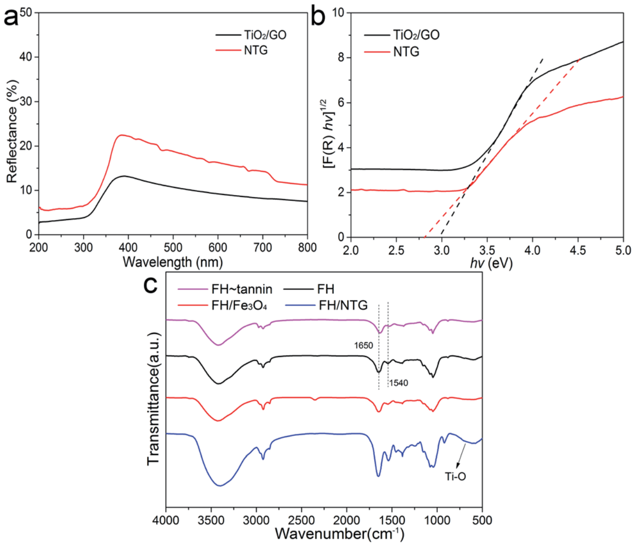

Fig. 5 (a) UV-Vis diffuse reflectance spectra of TiO_2/GO and NTG; (b) the corresponding plot of the transformed Kubelka–Munk function *versus* the light energy; (c) FTIR comparison of FH, FH–tannin, FH/Fe_3O_4, and FH/NTG.

Nevertheless, the intensities of characteristic bands in the FH/NTG spectra increased, indicating that the surface functional groups changed. In addition, the bands at 500–700 cm^{-1} presenting in the FH/NTG FTIR spectrum correspond to the Ti–O–Ti stretching vibration modes in crystalline TiO_2.[39]

3.2 The analysis of adsorption and photocatalysis

Fig. 6a shows ultraviolet spectra of tannin at different times. Two characteristic peaks of tannin can be seen at 215 and 275 nm. The decrease in the intensities of the peaks confirms the adsorption of tannin. Moreover, the concentration of tannin at different times was measured at 275 nm to determine the sorption kinetics of tannin on FTM. The inset image shows that the data fits well with both the pseudo-first-order and pseudo-second-order kinetics models, indicating that the adsorption of tannin could be a physical and chemical process. The pseudo-first-order and pseudo-second-order equations are as follows:

$$\ln(q_e - q_t) = \ln q_e - k_1 \tag{1}$$

$$t/q_t = 1/k_2 q_e^2 + t/q_e \tag{2}$$

where q_t and q_e correspond to the sorption amounts at time t and equilibrium, respectively. The terms k_1 (min^{-1}) and k_2 (g mg^{-1} min^{-1}) represent the adsorption rate constants of the pseudo-first-order and the pseudo-second-order models, respectively. The detailed model parameters are summarized in Table 1.

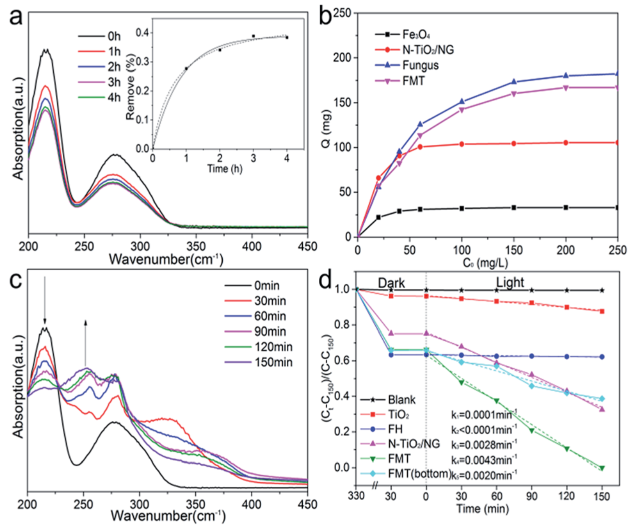

Fig. 6 (a) UV/Vis spectroscopy of the mixture in the dark; the inset image shows the kinetics of tannin adsorption on FTM; (b) the adsorption isotherms of Fe_3O_4, N-TiO_2/NG, fungus, and FMT; (c) UV/Vis spectroscopy of the reaction mixture under light irradiation; (d) a curve of photocatalytic degradation of tannin under visible light irradiation.

Fig. 6b shows the adsorption isotherms of Fe_3O_4, N-TiO_2/NG, fungus, and FMT at room temperature. The adsorption capacity of these samples follow the order: Fe_3O_4 < N-TiO_2/NG < FMT < FH. The adsorption capacity of Fe_3O_4 is far below that of N-TiO_2/NG and FH, suggesting that the compositions of FH and N-TiO_2/NG in FMT lead to the adsorption of tannin. FH shows the best adsorption of tannin among these samples and this is because the abundant polysaccharides, proteins, and phosphate groups on the surface of the FH cell walls cause various chemical and physical interactions between FH and tannin. For instance, the FTIR measurements of FH and FH–tannin (after adsorption of tannin), shown in Fig. 5c, indicate that the positions of the peaks at ~1540 and ~1650 cm^{-1}, which are assigned to the amine groups, undergo a red shift after the adsorption of tannin, due to the hydrogen-bonding interaction between FH and tannin.[40] Furthermore, the significant adsorption by N-TiO_2/NG in FMT could be generated because the graphene oxide derivatives, such as carbonyl, epoxy, and hydroxyl groups, enable it to interact with tannin. The aromatic rings of graphene and tannin suggest the formation of π–π stacking.[41] In addition, the amine groups on the surface of graphene, originating from the process of N-doping, also contribute to the sorption of tannin.

The high adsorption capacity for tannin means a larger concentration of tannin on the surface of FMT, which is conducive to photocatalysis. Therefore, the tannin can be effectively degraded into small molecules under simulated solar light. Fig. 6c shows the UV/Vis spectra of the reaction mixture within 150 min under simulated sunlight. It can be seen that a continuously decreasing peak at 215 nm confirms the degradation of tannin, while an increasing peak at 255 nm, which is absent at the beginning, illustrates a new compound formed after light irradiation.

Fig. 6d shows the photocatalytic degradation of tannin with TiO_2, FH, N-TiO_2/NG, FMT, and FMT(bottom) in static solution under simulated sunlight. The ordinate is set as $(C_t - C_{150})/(C - C_{150})$ to achieve an intuitive expression. C_t is the concentration of tannin at time t and C is the initial concentration. C_{150} is the concentration of tannin degraded by FMT at 150 min. No clear decrease in tannin was shown by the blank curve (no catalyst), indicating the stability of tannin under visible light irradiation. It is noted that the quantity of tannin decreased sharply during the first 5 h of the enrichment of tannin on the surface of the samples, and FH absorbed the most tannin, corresponding to the results of the absorption analysis. With simulated sunlight

Table 1 Absorption kinetics of pseudo first-order and second-order models

	Pseudo-first-order			Pseudo-second-order		
Sample	q_e (mg L^{-1})	k_1 (h^{-1})	R^2	q_e (mg L^{-1})	k_2 (g mg^{-1} h^{-1})	R^2
FTM	38.93	1.196	0.996	45.61	0.147	0.996

irradiation, the decreased concentrations of tannin confirmed its degradation. For a further study, the data for these samples is analysed by linear fitting, and the parameters (k) that are proportional to the reaction rates are calculated as follows: $k_1 = 0.0001\ \text{min}^{-1}$ (TiO$_2$), $k_2 < 0.0001\ \text{min}^{-1}$ (FH), $k_3 = 0.0028\ \text{min}^{-1}$ (N-TiO$_2$/NG), $k_4 = 0.0043\ \text{min}^{-1}$ (FMT), and $k_5 = 0.0020\ \text{min}^{-1}$ (FMT(bottom), FMT was forced to the bottom of the beaker by magnetic attraction). The photocatalytic performance of TiO$_2$ under visible light is poor, but is greatly enhanced after doping of nitrogen and the introduction of graphene. The low reaction rate with FH demonstrates that tannin cannot be degraded by FH, and the high content of FH on FMT(bottom) mainly leads to a lower photocatalytic performance compared to that of N-TiO$_2$/NG. It can be noted that the photocatalytic performance of FMT(bottom) is far more than can be accounted for by the content of N-TiO$_2$/NG in FMT(bottom), which indicates that some synergistic effects resulted from the combination of FH and N-TiO$_2$/NG. Comparing FMT(bottom) and FMT, the significant difference in their performances indicates that the floating state in this work is beneficial for photocatalysis.

4. Conclusions

In summary, functional FMT, which is a three-layered structure, was prepared by a simple, environmentally friendly co-culture method. The magnetic characteristics resulting from the introduction of nano-Fe$_3$O$_4$ are beneficial with respect to recycling FMT without secondary pollution. Moreover, a superior adsorption ability is obtained due to the functional groups from the FH and N-TiO$_2$/NG in FMT. The photocatalytic performance under solar light displays the degradation of tannin with N-TiO$_2$/NG. In addition, its high availability and ease of production make FMT suitable as a potential material for water treatment.

Acknowledgements

This work was financially supported by the Graduate School of CAEP, CAEP Institute of Technology, Laboratory for Extreme Conditions Matter Properties, Southwest University of Science and Technology, State Key Laboratory of Clean Energy Utilization of Zhejiang University and the Key Lab. for Power Machinery and Engineering of M. O. E. of Shanghai Jiao Tong University.

Notes and references

1 O. K. Varghese, M. Paulose, T. J. Latempa and C. A. Grimes, *Nano Lett.*, 2009, **9**, 731–737.
2 J. Yu, Y. Wang and W. Xiao, *J. Mater. Chem. A*, 2013, **1**, 10727–10735.
3 J. Yang, X. Zhang, B. Li, H. Liu, P. Sun, C. Wang, L. Wang and Y. Liu, *J. Alloys Compd.*, 2014, **584**, 180–184.
4 W. A. Velema, W. Szymanski and B. L. Feringa, *J. Am. Chem. Soc.*, 2014, **136**, 2178–2191.
5 R. R. Lew, *Nat. Rev. Microbiol.*, 2011, **9**, 509–518.
6 A. Sugunan, P. Melin, J. Schnürer, J. G. Hilborn and J. Dutta, *Adv. Mater.*, 2007, **19**, 77–81.
7 L. Zhang, Y. Wang, B. Peng, W. Yu, H. Wang, T. Wang, B. Deng, L. Chai, K. Zhang and J. Wang, *Green Chem.*, 2014, **16**, 3926–3934.
8 L. Zhang, *Nano Energy*, 2015, **17**, 224–232.
9 N. C. Bigall, M. Reitzig, W. Naumann, P. Simon, K. H. van Pée and A. Eychmüller, *Angew. Chem., Int. Ed.*, 2008, **47**, 7876–7879.
10 L. Du, Q. Xu, M. Huang, L. Xian and J. X. Feng, *Mater. Chem. Phys.*, 2015, **160**, 40–47.
11 W. Cheng, C. Ding, Y. Sun and X. Wang, *Chem. Eng. J.*, 2015, **269**, 1–8.
12 X. Xu, L. Xia, Q. Huang, J. D. Gu and W. Chen, *Environ. Technol.*, 2012, **33**, 1661–1670.
13 A. Ahmad, P. Mukherjee, S. Senapati, D. Mandal, M. I. Khan, R. Kumar and M. Sastry, *Colloids Surf., B*, 2003, **28**, 313–318.
14 A. M. Fontes, R. Geris, A. V. D. Santos, M. G. Pereira, J. G. S. Ramalho, A. F. D. Silva and M. Malta, *Biomater. Sci.*, 2014, **7**, 956–960.
15 K. B. Narayanan and N. Sakthivel, *Adv. Colloid Interface Sci.*, 2010, **156**, 1–13.
16 B. Volesky, *Water Res.*, 2007, **41**, 4017–4029.
17 Y. Sun, Q. Wang, C. Chen, X. Tan and X. Wang, *Environ. Sci. Technol.*, 2012, **46**, 6020–6027.
18 T. D. Nguyen-Phan, V. H. Pham, E. W. Shin, H. D. Pham, S. Kim, S. C. Jin, E. J. Kim and S. H. Hur, *Chem. Eng. J.*, 2011, **170**, 226–232.
19 L. Liu, Z. Liu, A. Liu, X. Gu, C. Ge, F. Gao and L. Dong, *ChemSusChem*, 2014, **7**, 618–626.
20 Y. Zhao, X. Qiu and C. Burda, *Chem. Mater.*, 2008, **20**, 2629–2636.
21 C. Liu, L. Zhang, R. Liu, Z. Gao, X. Yang, Z. Tu, F. Yang, Z. Ye, L. Cui and C. Xu, *J. Alloys Compd.*, 2015, **656**, 24–32.
22 L. Li, M. Xu, M. Chubik, M. V. Chubik, A. Gromov, G. D. Wei and W. Han, *RSC Adv.*, 2015, **5**, 41611–41616.
23 Q. Zhang, T. Lu, D. M. Bai, D. Q. Lin and S. J. Yao, *Chem. Eng. J.*, 2015, **284**, 972–978.
24 L. Chai, Y. Wang, N. Zhao, W. Yang and X. You, *Water Res.*, 2013, **47**, 4040–4049.
25 T. Wang, L. Zhang, C. Li, W. Yang, T. Song, C. Tang, Y. Meng, S. Dai, H. Wang and L. Chai, *Environ. Sci. Technol.*, 2015, **49**, 5654–5662.
26 P. J. Vikesland, A. M. Heathcock, R. L. Rebodos and K. E. Makus, *Environ. Sci. Technol.*, 2007, **41**, 5277–5283.
27 W. S. Hummers and R. E. Offeman, *J. Am. Chem. Soc.*, 1958, **80**, 1339.
28 S. Linley, Y. Y. Liu, C. J. Ptacek, D. W. Blowes and F. X. Gu, *ACS Appl. Mater. Interfaces*, 2014, **6**, 4658–4668.
29 L. Kumaresan, A. Prabhu, M. Palanichamy, E. Arumugam and V. Murugesan, *J. Hazard. Mater.*, 2011, **186**, 1183–1192.
30 C. Chen, W. Cai, M. Long, B. Zhou, Y. Wu, D. Wu and Y. Feng, *ACS Nano*, 2010, **4**, 6425–6432.
31 Y. Wang, J. Yu, W. Xiao and Q. Li, *J. Mater. Chem. A*, 2014, **2**, 3847–3855.
32 Y. Zhang, W. Zhu, X. Cui, W. T. Yao and T. Duan, *CrystEngComm*, 2015, **17**, 757–762.

33 Y. Cong, J. Zhang, F. Chen, A. Masakazu Anpo and D. He, *J. Phys. Chem. C*, 2007, **111**, 10618–10623.

34 F. Pei, Y. Liu, S. Xu, L. Jing, C. Wang and S. Cao, *Int. J. Hydrogen Energy*, 2013, **38**, 2670–2677.

35 V. Etacheri, J. E. Yourey and B. M. Bartlett, *ACS Nano*, 2014, **8**, 1491–1499.

36 Y. Tang, D. Wu, S. Chen, F. Zhang, J. Jia and X. Feng, *Energy Environ. Sci.*, 2013, **6**, 2447–2451.

37 W. Cheng, M. Wang, Z. Yang, Y. Sun and C. Ding, *RSC Adv.*, 2014, **4**, 61919–61926.

38 A. R. Badireddy, S. Chellam, P. L. Gassman, M. H. Engelhard, A. S. Lea and K. M. Rosso, *Water Res.*, 2010, **44**, 4505–4516.

39 B. Jiang, C. Tian, W. Zhou, J. Wang, Y. Xie, Q. Pan, Z. Ren, Y. Dong, D. Fu and J. Han, *Chem.–Eur. J.*, 2011, **17**, 8379–8387.

40 W. Li, W. Yao, W. Zhu, C. Xi and T. Duan, *J. Radioanal. Nucl. Chem.*, 2016, 1–10.

41 E. Lee, J. Y. Hong, H. Kang and J. Jang, *J. Hazard. Mater.*, 2012, **219–220**, 13–18.